Effects of As-Received Defects on Ceramic Matrix Composites Properties Using High-Fidelity Microstructures with Periodic Boundary Conditions

KHALED H. KHAFAGY and ADITI CHATTOPADHYAY

ABSTRACT

The presence of microstructural defects in as-received specimens of ceramic matrix composites (CMCs) significantly influences their constitutive response and damage, highlighting the importance of characterization and quantification of these defects for accurate assessment of damage and failure in the service environment. In a recent effort, the authors developed an algorithm to generate stochastic representative volume elements (SRVEs) of Carbon fiber Silicon-Carbide-Nitride matrix (C/SiNC) CMCs based on extensive multiscale material and defect characterization data. This paper implements this algorithm within a commercial finite element solver with periodic boundary conditions (PBCs) for high-fidelity micromechanics analysis and investigation of macroscopic material behavior of C/SiNC composites. Different loading directions are used to predict the global mechanical properties, and the results are in excellent agreement with theoretical (rule of mixture) predictions. Subsequently, the effects of as-received defects on the global and local responses are investigated. The results show that intratow porosity has pronounced degradation effects on the global elastic properties and results in complex stress localization patterns, which can be attributed to potential damage initiation sites.

INTRODUCTION

The superior characteristics of ceramic matrix composites (CMCs), such as low weight, high strength and toughness, and effective thermal properties, make them an ideal choice for extreme high-temperature applications [1- 2]. However, their complex morphologies, microstructures, manufacturing-related defects, and multiple failure modes make accurate predictions of material performance and residual useful life under service conditions challenging [3- 4]. The microstructural defects such as voids in the as-received CMC specimens stem from commonly employed manufacturing processes and variations in the constituents' thermal properties. The size, distribution, and morphology of the voids significantly impact the macroscopic constitutive behavior, thus highlighting the importance of characterizing defects across multiple length scales [3, 5- 6] and incorporating the information in physics-based multiscale models.

School for Engineering of Matter, Transport, and Energy, Arizona State University, Tempe, AZ, 85281, USA

Gowayed et al. conducted a characterization study and utilized an analytical model to study the influence of material defects on the elastic properties of two systems of SiC/SiC and one oxide/oxide CMCs [7]. The elastic properties were shown to deteriorate with increasing defects volume fraction (VF). Santhosh et al. used spheroidal inclusions with a micromechanics-based progressive damage model to predict the effects of porosity on the elastic properties of CG-Nicalon/SiNC CMCs [8]. Their results showed a more significant knockdown in the through-thickness modulus compared to the in-plane modulus. Although analytical models, such as Mori–Tanaka mean-field homogenization approach [9], can efficiently predict the homogenized properties of heterogeneous materials, they are unable to accommodate the effect of geometrical variations of constituent materials and capture the critical load transfer characteristics and damage mechanisms at lower length scales due to their idealized assumptions. In a recent effort, the authors have conducted an in-depth investigation of as-produced defects in C/SiNC CMC at multiple length scales using several experimental techniques, such as laser scanning microscopy, scanning electron microscopy (SEM), and energy dispersive spectroscopy (EDS) [5]. The primary classes of these defects were denuded matrix, interlaminar separations, open porosity, shrinkage cracks, and intratow porosity. An algorithm was also developed to generate stochastics representative volume elements (SRVEs) accounting for material variabilities such as inter- and intratow porosity and fiber VFs, fiber radii, intratow spacing, average tow size, and shape, size, VF, and distribution of defects, to facilitate high-fidelity multiscale physics-based modeling linking the constituent properties and subscale features to CMCs response.

In micromechanics, periodic boundary conditions (PBCs) are commonly utilized to model a periodic microstructure as a material point and obtain the effective properties of the material. Several authors developed and reported PBC algorithms for periodic RVEs in ABAQUS [10- 12]. Omairey et al. have reported a detailed algorithm for calculating material effective elastic properties [10]. However, this algorithm is computationally expensive and was limited to mechanical loadings. Tian et al. have developed a simple 3D PBC algorithm, where the authors conducted thermal simulations and discussed the calculation of effective thermal conductivities [11]. This paper discusses implementing a 3D PBC algorithm in ABAQUS for SRVEs under mechanical and thermal loading conditions. The PBCs are implemented via a linear multi-point constraint equation, which requires a linear combination of nodal degree of freedom (DoF) equated to zero. The procedure to calculate the effective material properties under different loading conditions (thermal and mechanical) is also discussed. The developed approach is combined with the previously developed multiscale SRVEs generation algorithm to investigate the effects of varying VF of defects on material properties and localized stress/strain distributions. This is particularly important since high-fidelity SRVE results of unidirectional CMCs are not readily available in the published literature. Since the SRVE algorithm utilizes an orthogonal structured mesh, its fidelity is first compared with traditional non-orthogonal finite element (FE) mesh. The SRVEs are then subject to different loading directions to compute elastic properties; the results are validated with the theoretical rule of mixture-based predictions.

Implementation of high-fidelity SRVEs in ABAQUS

The open-source DREAM.3D package, which allows for customized workflows to visualize multidimensional and multimodal data [13], is used to construct FE discretized microstructures generated using the previous developed SRVE generation algorithm. The FE discretized SRVEs are directly implemented within the commercial ABAQUS FE solver. Note that the SRVE generation algorithm generates orthogonal grid microstructures, where first, the composite domain is discretized, then the constituent geometry is assigned based on the mesh constraint [5]. However, in FE solvers such as ABAQUS (non-orthogonal grid), the constituent geometry is modeled first, and the domain is then meshed based on the geometric boundary constraints. Therefore, to verify the accuracy of the SRVE algorithm implementation in ABAQUS, a comparison of linear elastic FE simulations was conducted for single fiber RVEs obtained from the developed SRVEs generation algorithm (orthogonal grid) and ABAQUS (non-orthogonal grid). The fiber VF is 48%. The lower boundaries of the microstructure were fixed, and a force was applied to the upper boundaries. It is to be noted that the same grid size was used in both geometries. The results obtained using both geometries are in excellent agreement, as shown in Fig. 1. Figures 1a and 1b show contours of effective von Mises stress and Figs. 1c and 1d show contours of in-plane shear stress in orthogonal and non-orthogonal grids, respectively. While the results show excellent agreement between both geometries, the orthogonal grid microstructure does not show a smooth surface on the fiber-matrix interface due to the orthogonal elements. As a result, stress/strain was localized on the fiber-matrix interface. This can be improved with smaller mesh sizes. While the current implementation is demonstrated for FE analysis, the SRVE can also be simulated using other semi-analytical models such as the high-fidelity generalized method of cells (HFGMC) [14].

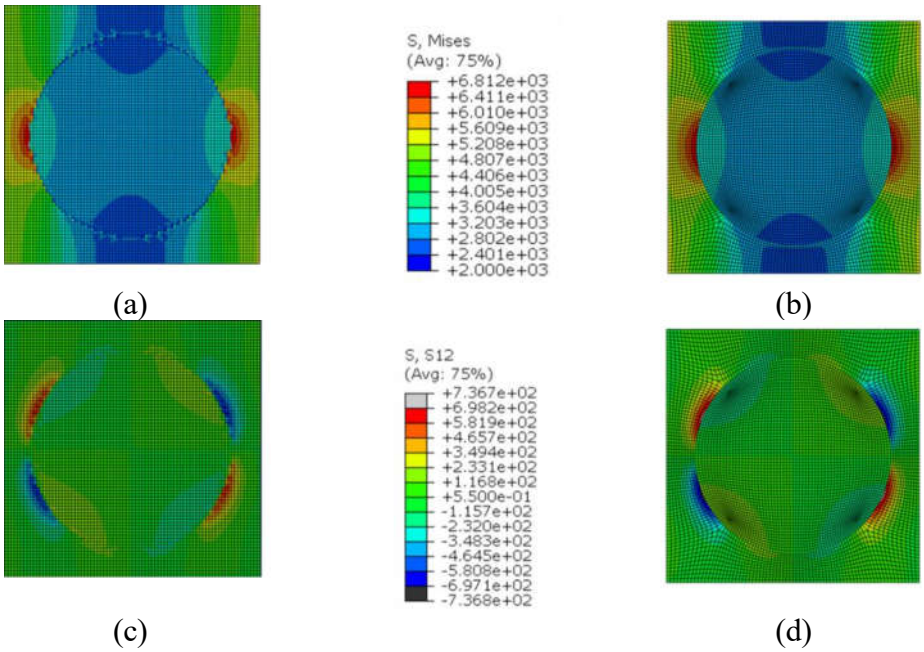

Fig 1. Single fiber matrix SRVE with 48% VF and fixed lower sides boundary conditions; Von-Mises results (in MPa) of (a) orthogonal and (b) non-orthogonal grid microstructures and in-plane shear stress (in MPa) of (c) orthogonal and (d) non-orthogonal grid microstructures

Implementation of periodic boundary conditions in ABAQUS

In micromechanics-based modeling or direct numerical simulation (e.g., FE), the application of PBCs to SRVEs idealizes them as material points over which the conjugate fields (e.g., stress and strain) are assumed to be uniform. The application of PBCs idealizes the SRVE as infinitely repeating in the directions in which periodicity is considered and allows the extraction of effective properties via volume averaging.

In this study, PBCs are implemented in ABAQUS via a linear multi-point constraint equation, which requires a linear combination of nodal DoF equated to zero. It also requires the nodes on opposite faces to be coupled to ensure the displacement periodicity and account for the applied strain or displacement. Equation (1) shows a generalized linear constraint equation, where a_i is a coefficient to define the relative motion of nodes and u_i is the DoF. Please note that in ABAQUS, DoF of displacement along x, y, and z are 1, 2, and 3, respectively, and temperature DoF is 11. The PBCs are introduced to SRVEs through reference points (RPs), whereas in 3D SRVE, three RPs should be defined for the three directions, see Table (1). Equation (2) shows an example of couple displacements of two opposite sides along *i*-direction, one side (u_{i^+}) and the other side (u_{i^-}) through the RP with a displacement value of Δu.

$$a_i u_i + a_j u_j + a_k u_k + a_l u_l + \cdots + a_m u_m = 0 \quad (1)$$

$$u_{i^+} + u_{i^-} = u_{RP}, \text{ and } u_{RP} = \Delta u \quad (2)$$

In 3D SRVEs, there are six faces/surfaces, and their corresponding nodes should be coupled along with all directions. However, edges of SRVEs are shared by multiple faces, and, likewise, corners are shared by multiple edges and faces. Coupling the same edge/node more than once to its opposite node will result in over constrains [10]. Consequently, developing an algorithm to capture these three sets (faces, edges, and vertices) is crucial. In the developed PBC algorithm, these three sets are extracted and stored independently. For instance, in Fig 2, the top face (face *1-2-3-4*) can be extracted and stored as all nodes at the top surface (surface *1-2-3-4*) except the four edges (including the red edge) and vertices (*1, 2, 3,* and *4*).

Similarly, in Fig 2, edges such as the red edge can be extracted as all nodes at edges *2-3* except vertices 2 and 3. To facilitate the application of arbitrary displacement-controlled loading to SRVEs, an RP should be defined along each direction (i.e., x, y, and z). In the same way, for thermal simulations and calculating the effective thermal conductivity, only one RP with temperature DoF should be utilized. In this case, displacements at Eq. (2) should be replaced by temperature.

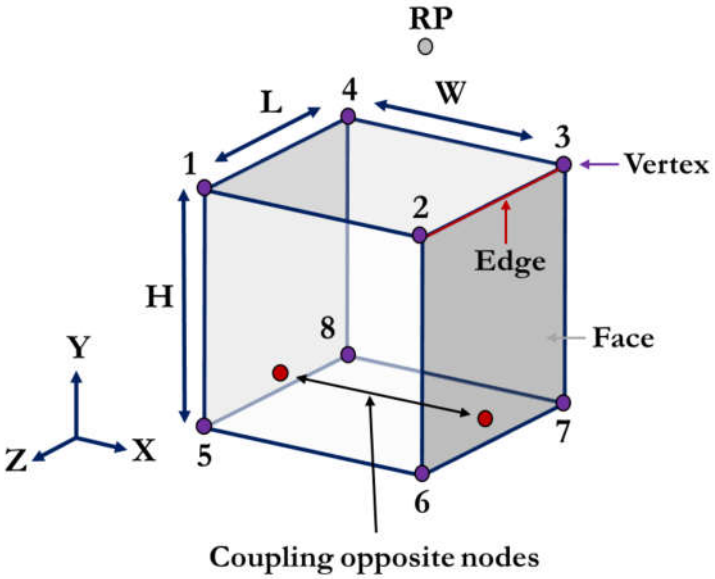

Fig 2. Schematic figure showing how the PBC algorithm extract and store different sets such as faces, edges, and vertices in a simple cubic RVE

The following section shows all linear equation constraints used in ABAQUS. Please note that the illustrative figure (Fig. 2) illustrates the coupling in the following equations. For example, u^{1234} refers to a displacement applied on all nodes of the upper face or face *1-2-3-4*, similarly u^{23} refers to a displacement applied on all nodes of the red edge or edge *2-3*, and u^{1} refers to the displacement applied on vortex *1*. The reference points can be defined arbitrarily outside the SRVE domain.

Faces:

Coupling faces along the Y-axis:

$$u^{1234} - u^{5678} = u^{RP2} \tag{3}$$

Coupling faces along the X-axis:

$$u^{3487} - u^{2156} = u^{RP1} \tag{4}$$

Coupling faces along the Z-axis:

$$u^{1485} - u^{2378} = u^{RP3} \tag{5}$$

Edges:

Coupling edges along the Y-axis:

$$u^{14} - u^{58} = u^{RP2} \tag{6}$$

$$u^{87} - u^{43} = u^{RP2} \tag{7}$$

Coupling edges along the X-axis:

$$u^{23} - u^{14} = u^{RP1} \tag{8}$$

$$u^{58} - u^{67} = u^{RP1} \quad (9)$$

$$u^{26} - u^{15} = u^{RP1} \quad (10)$$

$$u^{48} - u^{37} = u^{RP1} \quad (11)$$

Coupling edges along the Z-axis:

$$u^{15} - u^{48} = u^{RP3} \quad (12)$$

$$u^{56} - u^{87} = u^{RP3} \quad (13)$$

$$u^{12} - u^{43} = u^{RP3} \quad (14)$$

Vertices:

Coupling vertices along the Y-axis:

$$u^{4} - u^{8} = u^{RP2} \quad (15)$$

Coupling vertices along the X-axis:

$$u^{4} - u^{3} = u^{RP1} \quad (16)$$

$$u^{7} - u^{8} = u^{RP1} \quad (17)$$

Coupling vertices along the Z-axis:

$$u^{1} - u^{4} = u^{RP3} \quad (18)$$

$$u^{5} - u^{8} = u^{RP3} \quad (19)$$

$$u^{7} - u^{6} = u^{RP3} \quad (20)$$

$$u^{2} - u^{3} = u^{RP3} \quad (21)$$

A single fiber SRVE is generated from the developed SRVE generation algorithm to validate the accuracy of coupling equations in ABAQUS, as shown in Fig 3. The upper subfigures in Fig. 3 show 2D and 3D views of a single fiber SRVE with a domain size of 40 x 40 x 20 grids. The lower subfigures in Fig. 3 also show the sets corresponding to specific faces, edges, and vertices. For each set (faces, edges, and vertices), one node was selected to show the algorithm's accuracy; see orange nodes in each subfigure.

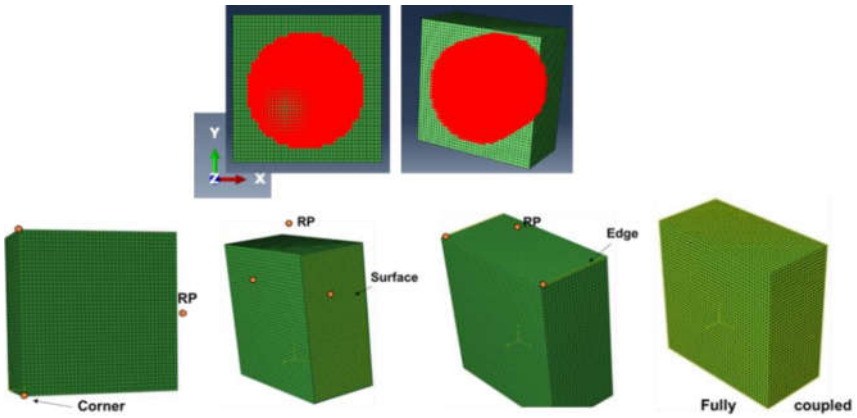

Fig 3. A single fiber matrix SRVE geometry highlighting the different sets in the PBC algorithm (faces, edges, and vertices)

Next, RPs are introduced in the FE model to couple the DoF of node sets (faces, edges, and vertices) along each principal direction (see Fig. 3). For instance, applying load on RP1 means applying load along x-direction, and RP2 and RP3 are the corresponding RPs along the y- and z-axis. The SRVE with the RPs is subject to six independent load paths (three normal directions and three shear directions) to obtain the 3D effective (homogenized) elastic material properties such as Young's and shear moduli and Poisson's ratio. Table (1) lists all required displacement BCs to calculate the effective material properties.

TABLE 1. Displacement boundary conditions of the PBC algorithm

	RP1			RP2			RP3		
	u_{xx}	u_{xy}	u_{xz}	u_{yx}	u_{yy}	u_{yz}	u_{zx}	u_{zy}	u_{zz}
E11	value	0	0	0	-----	0	0	0	----
E22	----*	0	0	0	value	0	0	0	----
E33	----	0	0	0	----	0	0	0	value
G12	0	value	0	value	0	0	0	0	0
G13	0	0	value	0	0	0	value	0	0
G23	0	0	0	0	0	value	0	value	0

*---- : No constraints are required

From the results of each simulation, the reaction forces and displacements are calculated at the corresponding RP, and the stress and strain are obtained accordingly based on the cross-sectional area and domain size. The Young's modulus and Poisson's ratio are calculated correspondingly. Since the experimental results are available only for constituents (fiber and matrix), the theoretical rule of mixture (RoM) was used to compare against the numerical results. Note that the RoM is known to underestimate matrix-dominated properties (e.g., the transverse Young's modulus) of composite materials but provides reasonably accurate predictions for fiber-dominated properties. In this paper, both matrix and fiber were assumed to be isotropic, and the material properties are listed in Table 2. Equations (23-25) show an example for calculating the homogenized material properties of the SRVE. Figure 4 shows the material properties at different SRVE mesh accuracy and fiber VFs. Where the results of Young's modulus along the fiber directions (E_{33}) show excellent agreement compared to the theoretical RoM. G_{12} and G_{23} show compatible results with different SRVE accuracy; however, theoretical RoM underestimates the shear modulus compared to the numerical results as discussed earlier.

$$E_{11} = \frac{RF_{x\,(RP1)}/(L \times H)}{u_{x\,(RP1)}/W} \tag{23}$$

$$G_{12} = \frac{RF_{x\,(RP2)}/(L \times W)}{\frac{u_{x\,(RP2)}}{H} + \frac{u_{y\,(RP1)}}{W}} \tag{24}$$

$$\nu_{12} = \frac{-u_{y\,(RP2)}/H}{u_{x\,(RP1)}/W} \tag{25}$$

Where *RF* and *u* refer to the reaction force and displacement at the RPs. L, W, and H are the cube dimensions as shown in Fig 2.

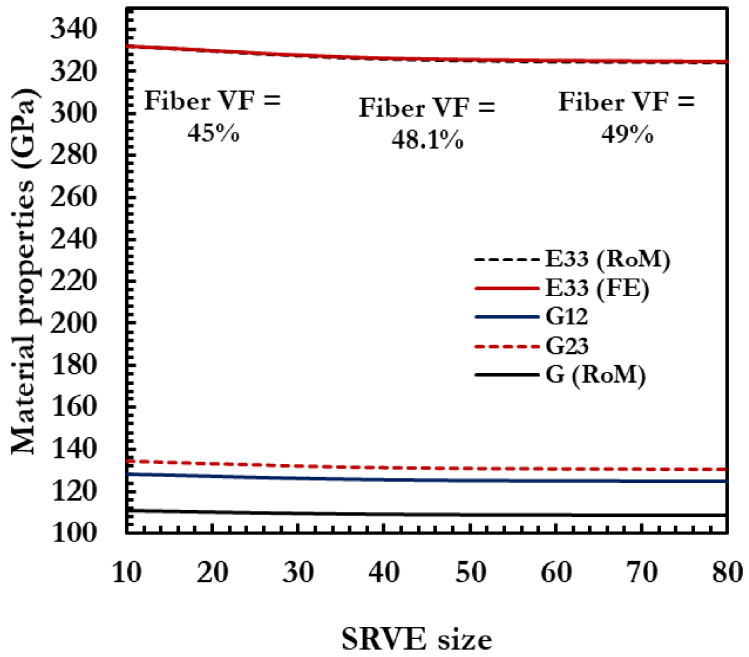

Fig 4. Homogenized material properties at different SRVE size and fiber VFs

TABLE 2. Elastic material properties for SiC and carbon T300 fibers [15]

	SiC	Carbon T300
$\boldsymbol{E}$ $\boldsymbol{(GPa)}$	415.0	230.0
$\boldsymbol{\nu}$	0.17	0.23

The effects of intratow porosity on C/SiC CMC properties

The SRVE generation algorithm is utilized with the developed PBC algorithm in ABAQUS to investigate the effects of as-produced defects on the material properties. SRVEs with dimensions of 60 × 60 × 20 grids, 48.9% fiber VF and different void VFs (from 0% to 5%) are used. Each SRVE is subject to six independent loadings to study the effects of the manufacturing-induced voids on all effective material properties. Figure 5 shows Young's and shear moduli degradation with increasing the void VF; see the secondary axis in Fig 5. Compared to the 0% (pristine), the longitudinal and transverse Young's moduli of the SRVE with 5% void VF degraded by 11.2% and 12.70%, respectively. The in-plane and through-thickness shear moduli also degraded by 13.29% and 13.99%, respectively. Due to the preferred location and distribution of voids with the matrix constituent, especially on the fiber-matrix interface, G_{12} showed the most degradation. Although the SRVE is heterogeneous due to the presence of

intratow voids, G_{13} and G_{23} have similar values as shown in Fig 5. The values of Poisson's ratios (ν_{13} and ν_{23}) increased at different void VFs based on the distribution and location of these voids.

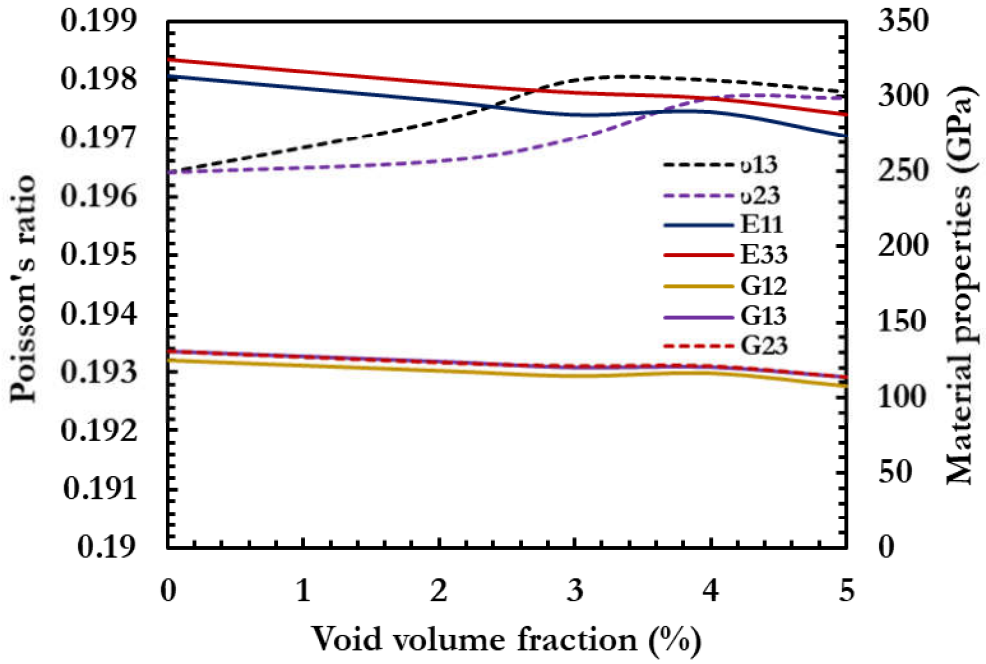

Fig 5. The influence of intratow porosity on the material properties using different voids VF SRVEs

While it is crucial to study the impact of voids on the material properties, it is also essential to investigate their influence on the stress/strain localization pattern. Consequently, the localization patterns could indicate potential damage and failure mechanisms simulated using physics-based inelastic simulations. Figures 6a and 6b show SRVEs with dimensions of $60 \times 60 \times 20$, 48.9% fiber VF, and 0% and 4% intratow porosity VFs, respectively. The SRVEs were loaded along the fiber direction (u_{zz}). The effective von-Mises stress contour of the SRVE without voids is shown in Fig 6a, where the contour has only two values for the fiber and matrix. After introducing the 4% intratow porosity VF, the stress localized around the voids creates hotspots resulting in a complex stress contour, as shown in Fig 6b. Figure 6b shows the stress contour of a 2D slice cut perpendicular to the fiber direction. In other sections, the coalescence between intratow voids results in localization bands in the matrix domain and at the interface due to intratow voids in its vicinity.

Moreover, the same SRVEs were utilized to investigate the effects of intratow voids on the shear modulus and the stress distribution pattern, where the SRVEs were loaded along the in-plane shear direction (u_{xy}). The effective von-Mises stress contour of the SRVE without voids is shown in Fig 7a, where the maximum stress localized around the fiber-matrix interface as expected during shear loads. Due to intratow voids, the effective von-Mises stress has a complex contour where the voids have around zero

value of stress (1.363×10^{-19} MPa) while maximum stresses were found to be localized around the voids, as shown in Fig 7b.

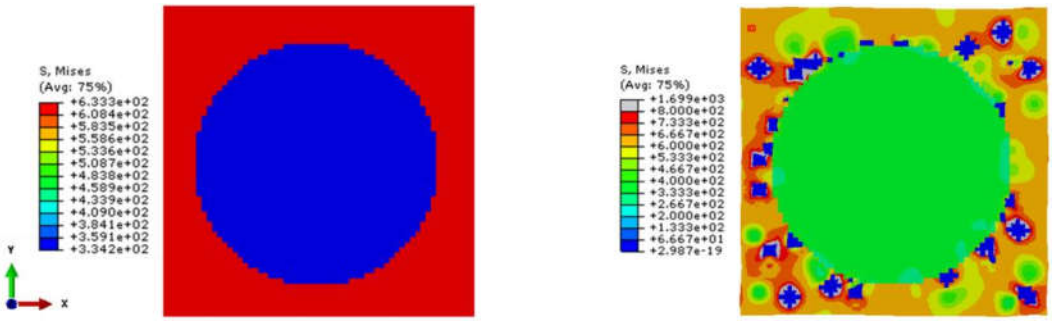

(a) (b)

Fig 6. Von-Mises stress contours of SRVEs, loaded along the fiber direction, with dimensions of $60 \times 60 \times 20$, 48.9% fiber VF, and (a) 0%; (b) 4%

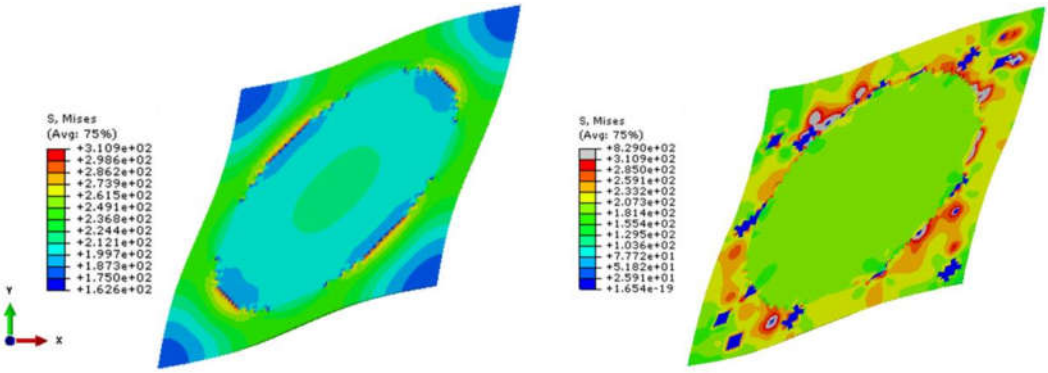

(a) (b)

Fig 7. Von-Mises stress contours of SRVEs, loaded along the in-plane shear direction, with dimensions of $60 \times 60 \times 20$, 48.9% fiber VF, and (a) 0%; (b) 4%

CONCLUSIONS

In this work, the authors utilized a recently developed SRVE generation algorithm for use in the multiscale simulation of C/SiNC CMCs. The algorithm was developed based on an extensive study of multiscale material characterization of structural and manufacturing defects in C/SiNC CMCs. This paper presents the development and implementation of a 3D PBC algorithm in ABAQUS. The SRVE and PBC algorithm were used to obtain the effective material properties and investigate the effects of intratow voids on the material properties and stress/strain distribution patterns under different loading directions. The numerical results along the fiber direction showed excellent agreement with the theoretical RoM model. However, the theoretical model underestimates the material properties on the transverse and shear directions compared to the numerical results, as expected. Different mesh size was used to ensure the convergence of the elastic material properties results. The elastic moduli degraded with increasing void VFs. Since the preferred location and distribution of intratow voids are near the matrix-fiber interface and in the matrix constituent, the stress concentration occurred around these voids, creating complex stress patterns and localization bands in the matrix domain. Consequently, these hotspots are expected to significantly affect the

damage initiation and failure mechanisms of the C/SiNC SRVEs subject to inelastic deformation.

ACKNOWLEDGMENTS

The research reported in this paper is supported in part by the Air Force Office of Scientific Research (Grant FA9550-18-1-00129, Project Manager: Jaimie Tiley), and the Department of Energy (Grant DE-FOA-0001993, Project Manager: Matthew F. Adams).

REFERENCES

[1] Zok, F.W., 2016. "Ceramic-matrix composites enable revolutionary gains in turbine engine efficiency," *Am. Ceram. Soc. Bull.* 95(5): 22-8.

[2] Valentine, P.G., Gradl, P.R., 2019. "Extreme-temperature carbon- And ceramic-matrix composite nozzle extensions for liquid rocket engines," *Int. Astronaut. Congr. (IAC)*, October 21, 2019.

[3] Mital, S., Goldberg, R. and Bonacuse, P., 2012. "Modeling of Damage Initiation and Progression in a SiC/SiC Woven Ceramic Matrix Composite," *53rd AIAA/ASME/ASCE/AHS/ASC Structures, Structural Dynamics and Materials Conference 20th AIAA/ASME/AHS Adaptive Structures Conference 14th AIAA*, April 2012.

[4] Goldsmith, M.B., Sankar, B.V., Haftka, R.T. and Goldberg, R.K., 2015. "Effects of microstructural variability on thermo-mechanical properties of a woven ceramic matrix composite," *Journal of Composite Materials*, 49(3): 335-350.

[5] Khafagy, K.H., Datta, S. and Chattopadhyay, A., 2021. "Multiscale characterization and representation of variability in ceramic matrix composites," *Journal of Composite Materials*, 55(18): 2431-2441.

[6] Skinner, T., Rai, A. and Chattopadhyay, A., 2020. "Multiscale ceramic matrix composite thermomechanical damage model with fracture mechanics and internal state variables," *Composite Structures*, 236: 111847.

[7] Gowayed, Y., Ojard, G., Prevost, E., Santhosh, U. and Jefferson, G., 2013. "Defects in ceramic matrix composites and their impact on elastic properties," *Composites Part B: Engineering*, 55: 167-175.

[8] Santhosh, U., Ahmad, J., Ojard, G., Smyth, I., Gowayed, Y. and Jefferson, G., 2020. "Effect of porosity on the nonlinear and time-dependent behavior of Ceramic Matrix Composites," *Composites Part B: Engineering*, 184: 107658.

[9] Mori, T. and Tanaka, K., 1973. "Average stress in matrix and average elastic energy of materials with misfitting inclusions," *Acta metallurgica*, 21(5): 571-574.

[10] Omairey, S.L., Dunning, P.D. and Sriramula, S., 2019. "Development of an ABAQUS plugin tool for periodic RVE homogenization," *Engineering with Computers*, 35(2): 567-577.

[11] Tian, W., Qi, L., Chao, X., Liang, J. and Fu, M.W., 2019. "Numerical evaluation on the effective thermal conductivity of the composites with discontinuous inclusions:

Periodic boundary condition and its numerical algorithm," *International Journal of Heat and Mass Transfer*, 134: 735-751.

[12] Barbero, E.J., 2013. "Finite element analysis of composite materials using Abaqus™," CRC press.

[13] Groeber, M.A. and Jackson, M.A., 2014. "DREAM. 3D: a digital representation environment for the analysis of microstructure in 3D," *Integrating materials and manufacturing innovation*, 3(1): 56-72.

[14] Khafagy, K.H., Venkatesan, K.R.R., Balusu, K., Datta, S. and Chattopadhyay, A., 2021. "Stochastic microstructural analysis of ceramic matrix composites using a high-fidelity multiscale framework," In AIAA Scitech 2021 Forum (p. 1350).

[15] Daniel, I.M., Ishai, O., Daniel, I.M. and Daniel, I., 2006. "Engineering mechanics of composite materials," (Vol. 1994). New York: Oxford university press.